Experimental Study of the Passive Control of the Pressure Oscillations in Large SRM

J. Anthoine and M. R. Lema
von Karman Institute for Fluid Dynamics
Chaussée de Waterloo 72, B1640 Rhode-Saint-Genèse, Belgium

Abstract

Cold gas experiments are used to study the pressure oscillations occurring in solid rocket motors (SRM). Previous studies stated that flow–acoustic coupling is mainly observed for nozzles including cavity. The nozzle geometry has an effect on the pressure oscillations through a coupling between the acoustic fluctuations induced by the cavity volume and the vortices travelling in front of the cavity entrance.

Passive control of the pressure oscillations is investigated by inserting a solid membrane at the entrance of the cavity to prevent the vortices to interact with the nozzle cavity. An analytical model is adapted for the passive control geometry to determine the attenuation factor of the pressure oscillations. Experiments performed in an axially injected cold flow model demonstrate that passive control with impermeable membrane produces the same pressure oscillations than when the cavity is not present. Passive control with a membrane with holes allows reducing the pressure oscillations compared to the case without passive control.

1. Introduction

The present research is an experimental investigation of the aeroacoustic instabilities occurring in a sub-scaled cold flow model of the Ariane 5 solid rocket motor. The phenomenon develops in the confined flow established in the motor and involves a coupling between hydrodynamic instabilities and longitudinal acoustic modes.

Aeroacoustic instabilities occur in a wide range of technical applications. The resulting oscillations are sometimes wanted in systems designed to produce the periodic motion efficiently as in musical instruments. Nevertheless, in most cases aeroacoustic instabilities perturb the operation, as for the Ariane 5 launcher. Then, the present research finds its interest knowing that these aeroacoustic instabilities lead to pressure and thrust oscillations which reduce the rocket motor performances and could damage the payload.

For technological reasons, large solid rocket motors are composed of a submerged nozzle and segmented propellant grains separated by inhibitors, as sketched in figure 1. During propellant combustion, a cavity appears around the nozzle. Vortical flow structures may be formed from the downstream inhibitor (Obstacle Vortex Shedding - OVS) or from natural instabilities of the radial flow resulting from the propellant combustion (Surface Vortex Shedding - SVS). The hydrodynamic manifestations drive pressure oscillations in the internal flow established in the motor. When the vortex shedding frequency synchronizes acoustic modes of the motor chamber, resonance may occur and sound pressure can be amplified by vortex-nozzle interaction, leading to pressure and thrust oscillations.

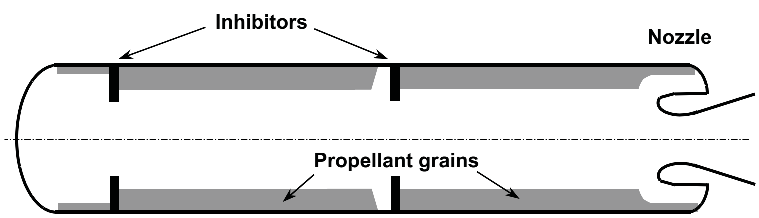

Figure 1: Internal geometry of the Ariane 5 solid rocket motor.

The stability prevision of large solid propellant rocket motors has been an active subject, both in the USA and in Europe, in the past twenty years. Although these motors were predicted stable by classical stability assessment methods,[1,2] such grain segmentation conducted to low amplitude, but sustained, pressure and thrust oscillations, on first longitudinal acoustic mode frequencies. These pressure oscillations have been reported for the Space Shuttle RSRM, the Titan-34D SRM, the Titan–IV SRMU and the Ariane 5 MPS.[2–6] All these boosters have a length over diameter ratio (L/D) in the range $9 - 12$ and demonstrated similar pressure oscillations, whatever the number of segments. Table 1 yields a comparison of the published vortex-induced oscillation data. Values are not reported in the literature for the Titan-34D SRM. Zero-peak relative amplitudes are typically less than 0.5% for pressure oscillations and less than 5% for thrust oscillations.

First acoustic mode	RSRM	SRMU	MPS
MPO (0-to-peak) [kPa]	–	16.2	25.5
MPO (0-to-peak) / mean pressure	0.0025	0.005	0.0027
Time of occurrence of MPO	70 – 75	57 – 64	90 – 95

Table 1: Comparison of the vortex-induced oscillation data. MPO stands for "maximum pressure oscillation". From.[5]

To support the development of the Ariane 5 P230/MPS solid motors, the CNES (Centre National d'Etudes Spatiales) conducted, from 1989 till 2000, the ASSM (Aerodynamics of Segmented Solid Motors) research program. The scientific methodology of the ASSM program was based on the understanding of the physical aspects, on their modeling and on the development of stability assessment tools. The objective of that program was to predict the pressure oscillation levels and frequencies. That ambitious objective needed to develop direct numerical simulation codes and to design cold flow experiments and static firing tests. Of course, the program was not limited to the investigation of the aeroacoustic instabilities. It was also addressed to the combustion instabilities, the flow-structure coupling, the two-phase flow coupling, among others.

In parallel, the von Karman Institute (VKI) worked between 1991 and 1996 on the identification of such pressure oscillations, from experiments on cold test bench, directly for the booster manufacturer (SNIA / BPD / Fiat Avio). With its experience, the von Karman Institute was asked by CNES to join the ASSM program to investigate and identify the origin of vortices within the combustion chamber and their acoustic coupling with the cavity located at the base of the solid rocket engine.[7] This investigation was performed theoretically, experimentally on cold test bench and numerically between 1996 and 2000 within the ASSM CNES program.[8] During that period, the VKI had the opportunity to collaborate with TU/e (Technical University of Eindhoven), SNPE (Société Nationale des Poudres et Explosifs), ONERA (Office National d'Etudes et de Recherches Aérospatiales), Ecole Centrale Paris and ENSMA (Ecole Nationale Supérieure de Mécanique et d'Aérotechnique).

2. Earlier works

Anthoine *et al.*[9] developed a non-linear model, based on vortex-sound theory, to point out the effect of the nozzle design on sound production. The model predicts that, when resonance occurs, the sound pressure level $|p'|/p_0$ (or P_{rms}/P_s in the figures of this report) is a linear function of the Mach number M_0[1], the excited mode number j and the nozzle cavity volume V_c:

$$\frac{|p'|}{p_0} \sim \frac{\pi\gamma}{\gamma - 1} j M_0 \frac{V_c}{V_{tot}} \tag{1}$$

where

$$V_{tot} = \frac{\pi D^2}{4} L \tag{2}$$

and where γ is the specific heat ratio, D is the internal diameter of the segments and L is the total length of the test section.

The results of this model are validated by experimental data. A weak point in the model is that it is assumed that the vortex trajectory remains independent of the geometry of the cavity. This will appear to be reasonable in the present case. Note furthermore that if the acoustical energy losses are not dominated by the radiation at the nozzle one will still find that $|p'| \sim V_c$ but not necessarily that $|p'| \sim M_0$.

The experiments are conducted on axisymmetric cold flow models respecting the Mach number similarity with the Ariane 5 SRM.[10–13] The test section includes only one inhibitor and a submerged nozzle. The flow is either created by an axial air injection at the forward end (figure 3a) or by a radial injection uniformly distributed along chamber porous cylinders (figure 3b). The internal Mach number can be varied continuously by means of a movable needle

[1] M_0 is the the longitudinal Mach number averaged across the cross-section of the segment

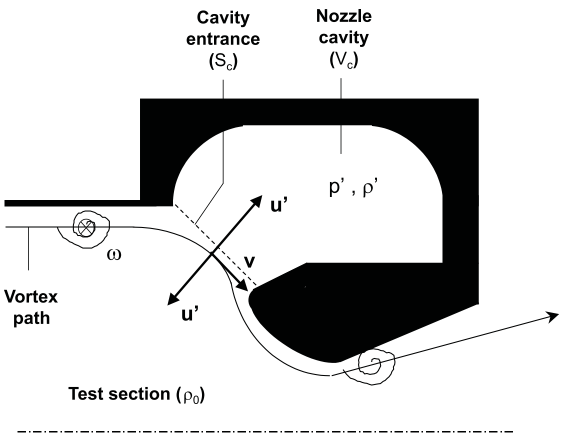

Figure 2: Theoretical modeling of the vortex-nozzle interaction.

placed in the nozzle throat. The acoustic pressure measurements are performed by piezoelectric transducers. The signal treatment yields the amplitude and the frequency of the pressure oscillations. The experimental facility with axial flow injection will be further described.

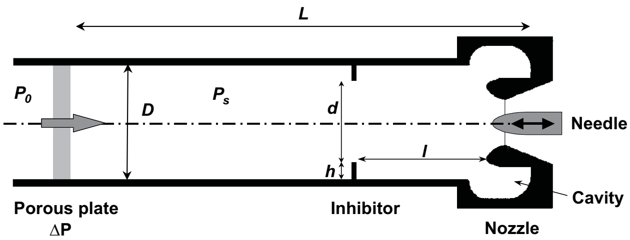

(a) Axial injection

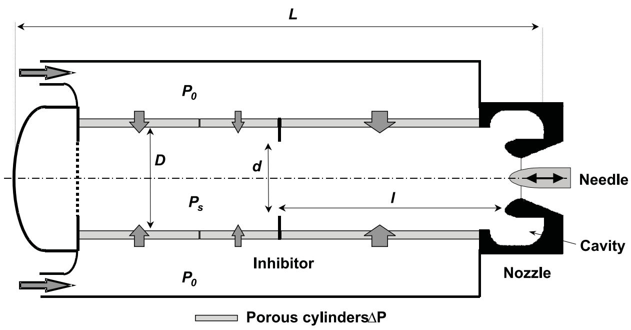

(b) Radial injection

Figure 3: Axial and radial cold flow set-ups (1/30-scale).

Plotting the contours of pressure fluctuation amplitudes versus Helmholtz number (representing frequency) and longitudinal Mach number (representing time[2]) identifies flow-acoustic coupling when the vortex shedding is coupled to one of the acoustic resonant modes of the test section, bringing the fluctuation level to large value (figure 4a). An extensive study of the effect of the nozzle cavity geometry has been made at VKI.[7] Flow-acoustic coupling is mainly observed for nozzles including cavity. The nozzle geometry has an effect on the pressure oscillations through a coupling between the acoustic fluctuations induced by the cavity volume and the vortices travelling in front of the cavity entrance (figure 4b). When resonance occurs, the sound pressure level increases linearly with the chamber Mach number, the frequency and the cavity volume. When removing the nozzle cavity, the pressure oscillations can be reduced by one order of magnitude. Such a finding is in good agreement with the analytical model.

[2]Since the combustion of solid propellant is radial, the internal diameter, and consequently the cross-section, of the solid segments is increasing

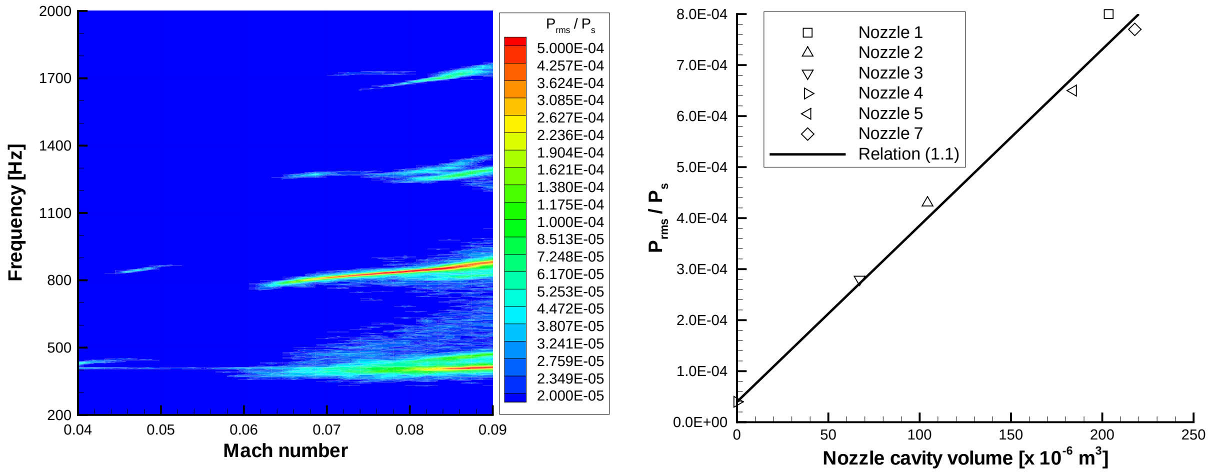

(a) Contour of pressure amplitude

(b) Maximum pressure levels with cavity volume

Figure 4: Major results of the experimental approach. Contour of pressure amplitude (a) and maximum pressure levels with cavity volume (b) for the axial injection.

3. Experimental facility

The experimental facility is a 1/30-scale modular axisymmetric cold flow model of the Ariane 5 solid rocket motor, with a fully axial flow. The VKI cold flow model provides exact geometric and Mach number similarity with the full-scale motor when 50% of the propellant is burnt. That mid-combustion condition corresponds to the maximum of pulsations. The Mach number, based on the mean flow velocity in the segments, is of the order of 0.1. Since the Reynolds number, based on the same velocity and on the segments diameter, is of the order of $2 \cdot 10^7$ in the full-scale motor, the viscous effects are negligible and do not influence the flow properties. Therefore, exact Reynolds number scaling is not required as long as it is large enough.

The facility consists of a cylindrical test section, with an inhibitor, and a submerged nozzle with sonic condition at the throat.[14,15] The experimental model is sketched in figure 3a. The internal diameter D of the segments is equal to 76 mm. The test section is made of 2 to 6 interchangeable segments of different lengths to make possible the variation of the total length L. This allows the influence of the Helmholtz number to be analyzed by varying the acoustic mode frequencies of the test section. The available lengths for the individual segments are 30, 55 and 85 mm and measurements are obtained for a total length ranging from 160 mm to 400 mm. The relative position of the inhibitor with regard to the total length can also be modified, providing investigation of different inhibitor-nozzle distances l. Three inhibitors of internal diameter d equal to 58, 62 and 68 mm are considered, although some tests are carried out without inhibitor. The inhibitors have a thickness of 1.5 mm and a sharp edge.

The test section is connected to a compressed air tank of 9.8 m^3 at 1.2 MPa. The temperature of the fluid in the test section is around 290 K, while the static pressure is varying between 170 kPa and 420 kPa depending on the Mach number. The minimum static pressure value guarantees sonic conditions at the nozzle throat. The exact temperature and pressure are controlled in real-time during each test campaign. The circulation of the air along all the connecting pipes produces acoustic noise that could interact with the acoustic measurements carried out in the test section. The insertion of a porous plate at the forward end aims to ensure an acoustic insulation of the test section from the air supply, by providing a high pressure drop.[16] This pressure drop is of the order of magnitude of the static pressure in the test section.

3.1 Nozzle geometry and needle system

The submerged 1/30-scale nozzle, with a throat diameter of 30 mm, whose detailed drawing is given in figure 5, is close to the geometry of the real one. The corresponding Mach number at the segments is equal to 0.09 and corresponds to mid-combustion (50% of the propellant burnt). The main characteristic of this nozzle is the appearance of a cavity around the convergent. During combustion, the cavity volume varies as explained in section 2. At 50 % of the combustion, the geometry is close to that drawn in figure 5a. Figure 5b provides a photography of the experimental

---

with time, which leads to a reduction of the Mach number with time. Mach number is then inversely proportional to time evolution.

submerged nozzle with its cavity. A similar nozzle with a throat diameter of 37 mm allows increasing the Mach number range. It presents the same submerged cavity and is used for most of the tests presented in this paper.

(a) Detailed drawing (b) Photograph

Figure 5: Detailed drawing and photograph of the submerged nozzle with the needle.

In the Ariane 5 booster, the flow-acoustic coupling is characterized by a shift of the instability mode frequency with respect to time and a frequency jump between the instability modes. Then, time evolution has to be considered in the experiments. As the combustion is radial, the internal Mach number in the segments varies as the inverse of time. To simulate correctly the Mach number evolution in a cold flow model, one should realize an axisymmetric test section whose internal diameter could increase with time. Such a behavior is technically difficult to achieve. The internal Mach number M_0 is defined by:

$$M_0 = \frac{U_0}{c_0} = \frac{\dot{m}}{\rho_f c_0} \tag{3}$$

where U_0 is mean axial velocity, c_0 is the speed of sound and ρ_f is the cold air density in the test section. As a sonic throat nozzle ends the test section, the mass flux $\dot{m}$ is given by:

$$\dot{m}S = \frac{AP_s}{c_0}\gamma\left(2\frac{1+\frac{\gamma-1}{2}M_0^2}{\gamma+1}\right)^{\frac{\gamma+1}{2(\gamma-1)}} = \gamma K\frac{AP_s}{c_0} \tag{4}$$

where S is the cross-area of the segments, A is the throat area and P_s is the static pressure in the test section. For small Mach number ($M_0 \sim 0.1$), K depends only on the specific heat ratio γ (for cold air, $K = 0.58$). Applying the definition of the speed of sound $c_0^2 = \gamma RT$ and the state equation $P_s = \rho_f RT$, where T is the static temperature and R is the gas constant for air, provides:

$$M_0 = K\frac{A}{S} \tag{5}$$

A pressure change in the segments affects the Reynolds number but does not modify the Mach number, as indicated by equation 5. So, the only way to vary the Mach number is to change the nozzle throat area A by using a movable needle, displaced along the axis of the nozzle (figure 3a). Then, instead of increasing the segments internal diameter with respect to time as for the Ariane 5 booster, the nozzle throat section is reduced. This difference should be kept in mind when discussing the results. Indeed, in the present sub-scale model, the geometry of the segments, of the inhibitor and of the nozzle lip are fixed. On the other hand, during the propellant combustion in the Ariane 5 booster, the diameter of the propellant interface varies compared to the inhibitor and nozzle throat diameters. Table 2 gives the nominal experimental conditions (without needle) and their range when the needles are used. They are also compared to the Ariane 5 full-scale booster parameters.

3.2 Instrumentation

The acoustic pressure fluctuations are measured with a piezoelectric transducer Model 106B50, called further PCB probe, connected to the amplifying power unit Model 483B08, both from PCB Piezotronics Inc. As the PCB probe can only measure pressure fluctuations, it is calibrated using a sinusoidal pressure generator (Model CA250 Precision Calibrator from Larson Davis). It gives a signal of 114 dB (ref. 20 μPa) at 250 Hz. In all the experiments, the PCB probe is placed just downstream the porous plate and is flush mounted on the wall of the test section. It corresponds to the "forward end" measurement point commonly used in solid rocket experiments.

	VKI model	Typical SRM 50 s (95 s)
D [m]	0.076	1.9 (2.6)
A [$\times 10^{-4}$m^2]	2.54 – 10.75	6400
d [m]	0.058 – 0.068	1.6 (1.8)
L [m]	0.13 – 0.393	24.1
l [m]	0.046 – 0.334	9.7
p_0 [$\times 10^5$Pa]	1.7 – 4.2	44 (49)
a [m $\cdot$ s^{-1}]	338	1085
M_0	0.03 – 0.14	0.13 (0.07)
Flow injection	axial	radial

Table 2: Comparison between cold flow experimental conditions and typical SRM parameters.

The static pressures upstream and downstream of the porous plate are used to control the sonic condition at the nozzle and to characterize the pressure drop at the porous plate. They are acquired using Validyne differential pressure transducers, model CD15, equipped with well adapted diaphragm.

The needle is moved by means of a step-by-step rotating motor. The needle position is measured with an optical turn counter placed on the motor axis and providing 360 pulses per turn. Each pulse corresponds to a vertical displacement of 0.00757 *mm*. Since the needle penetration length is equal to 24 mm and each test consists of 50 measurements points, the distance between them is 0.48 *mm*, which gives around 0.0014 variation of the Mach number. The needle displacement is synchronized with the data acquisition program. It means that the acquisition program starts only when the needle has reached one position. During the acquisition, the needle is not moving to guarantee constant Mach number. At the end of the acquisition, the needle motor restarts to move the needle to its next position. Knowing the needle penetration, the internal Mach number can be computed when sonic conditions at the nozzle throat are achieved.

The PCB acoustic pressure fluctuations are acquired by means of a DAS1601 acquisition card controlled by Testpoint. The signals from the PCB are first filtered at 3 kHz. The PCB signals are amplified by a factor 200 (gain of 10 at the PCB amplifying power unit and of 20 at the filter unit). As indicated above, an acquisition of the optical counter, of all the validynes and of the PCB is taken every 0.48 mm variation of the needle position. This is done 50 times to cover the complete range of the needle displacement, i.e. the complete range of the Mach number. At each needle step, the acquisition frequency of the PCB is 7.5 kHz and 65536 data points are saved on the hard disk. For the optical counter and for the validynes, only the average values are saved for each neeedle step. The 65536 PCB data points are analyzed to determine the power spectrum of the pressure fluctuations. All the computations are performed using the Matlab software. The spectrum is averaged on 15 blocks of 8192 data with an overlapping of 0.5. That gives a frequency resolution of 0.92 Hz.

4. Identification of flow-acoustic coupling

The flow-acoustic coupling has been defined in section 2. It is identified when

- the vortex shedding is occurring at an acoustic mode frequency of the chamber and is jumping between the acoustic modes ;
- the vortex shedding excites the acoustic properties of the test section ;
- the acoustic of the test section modifies the vortex shedding frequency evolution.

It is worth attempting to derive an analytical model to predict the conditions for the occurrence of flow-acoustic coupling. This model is based on Rossiter's approach.[17]

The generation of self-sustained sound resonance in a tube depends on the phase of the acoustic oscillation at which a vortex shed by the upstream obstacle reaches the downstream one.[18] This phase is determined by the time T_v needed by a vortex to travel the distance between the obstacles. In the present model, the upstream obstacle is the inhibitor while the downstream one is the nozzle. The advection time T_v of the vortices to cover the distance between the obstacles is given by[5]:

$$T_v = \frac{l}{U_v} = T(m - \alpha) \tag{6}$$

where l is the inhibitor-nozzle distance, U_v is the vortex transport velocity, $T = 1/f$ is the vortex shedding period and m is the number of vortices located between the inhibitor and the nozzle, called the stage number. $\alpha = 0.25$ is a correction factor that is justified hereafter.

Let us assume that vortex-nozzle interaction generates an acoustic wave. This wave will propagate and reflect at the closed upper end of the test section. If dissipation by vortex shedding at the inhibitor, pressure response of the porous plate and friction are neglected, the incident wave will interfere with the reflected wave to form a standing acoustic wave.[19] Figure 6 displays the acoustic velocity shapes for the two first longitudinal standing acoustic waves. The modes of the test section are approximate by that for a closed-closed chamber. Thus, the acoustic velocities are nil at both extremities.

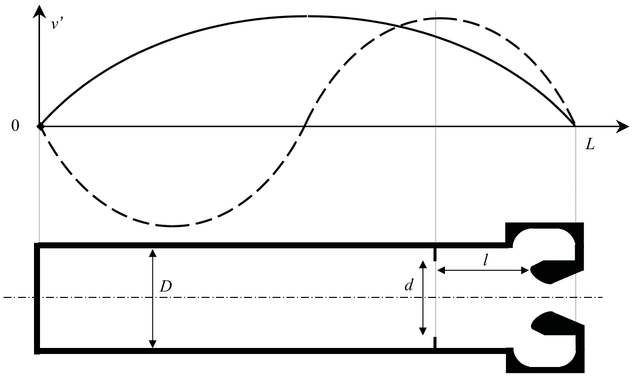

Figure 6: Acoustic velocity fluctuation shapes. ——— : first acoustic mode. – – – – : second acoustic mode. L = 393 mm ; l = 71 mm.

To facilitate coupling with an acoustic mode, vortices have to be shed near a pressure node (acoustic velocity antinode). Thus, the inhibitor should be close to an acoustic velocity antinode. The inhibitor position exemplified in figure 6 promotes excitation of the second acoustic mode as it is put in the cross-section of the acoustic velocity antinode for the second mode. Then, when vortices interact with the nozzle, sound is produced. This sound can be propagated by the acoustic mode only if it is generated near a velocity node (acoustic pressure antinode). Thus, the nozzle should be located close to an acoustic pressure antinode. Therefore, the vortex shedding at the inhibitor is assumed to be in phase with the acoustic velocity, while the source at the nozzle is in phase with the acoustic pressure. Since the acoustic velocity in a standing wave lags a quarter oscillation period behind the pressure oscillation,[5] introduced a correction factor $\alpha = 0.25$ in equation 6.

Equation 6 can also be written in term of a Strouhal number based on the vortex transport velocity:

$$Str_v = \frac{fl}{U_v} = m - 0.25 \tag{7}$$

At resonance, the vortex shedding frequency is equal to one of the acoustic mode frequencies:

$$f = f_{ac,j} = \frac{jc_0}{2L} \tag{8}$$

where j is the acoustic mode number, c_0 is the speed of sound and L is the total length of the test section. The vortex transport velocity U_v is related to the mean flow velocity U_0 upstream the inhibitor by:

$$U_v = k_v U_{jet} = \frac{k_v}{C_{vc}} \left(\frac{D}{d}\right)^2 U_0 = kU_0 \tag{9}$$

where k_v is the ratio of the vortex transport velocity U_v to the jet velocity U_{jet}. For a circular jet exhausting in an unbounded space, it is shown in the literature that the ratio k_v is equal to $0.5 - 0.6$.[20–22] When the jet exhausts in a pipe, like in our model, the surrounded wall slows down the vortices and the ratio k_v is reduced. C_{vc} is the “vena contracta” coefficient of the jet generated by the inhibitor.[23] D is the test section internal diameter and d is the inhibitor internal diameter. k is the ratio of the vortex transport velocity U_v to the velocity U_0 upstream the inhibitor. From the experimental investigation of the vortex properties,[7] $C_{vc} = 0.68$ and $k = 1.19$. Therefore, equation 9 leads to $k_v = 0.47$.

Finally, by combining equations 7 to 9, one gets a relation linking the Mach number M_0 to the excited mode number j, the stage number m, the relative position of the inhibitor compared to the total length of the test section l/L and to the relative internal diameter of the inhibitor compared to the test section diameter d/D:

$$M_0 = \frac{C_{vc}}{2k_v} \frac{j}{m - 0.25} \frac{l}{L} \left(\frac{d}{D}\right)^2 \tag{10}$$

When resonance occurs, the selection of the acoustic mode j depends on the relative position l/L of the inhibitor compared to the acoustic mode shape (figure 6). Indeed, to yield high sound pressure levels and to obtain a maximum of acoustic receptivity at the inhibitor, the inhibitor must be as close as possible to an acoustic pressure node (highest acoustic velocity fluctuations). Then, the coupling will occur for that acoustic mode only when an integer number of vortices m are present between the inhibitor and the nozzle. The flow-acoustic coupling will excite that acoustic mode with that number of vortices only for some Mach number M_0 depending on the geometrical parameters (l/L and d/D) so that relation 10 is respected.

Equation 10 can also be written in term of the Helmholtz number $He = fl/c_0$, based on the speed of sound:

$$He = M_0 \frac{k_v}{C_{vc}} \left(\frac{d}{D}\right)^2 (m - 0.25) \tag{11}$$

5. Example of flow-acoustic coupling

Figure 4a shows the pressure fluctuation spectrum plotted versus Mach number M_0 and frequency for an inhibitor of 58 mm internal diameter placed at 71 mm from the head of the submerged nozzle (Figure 5). Oscillation frequencies f are close to the resonance frequencies. In first approximation the acoustic standing wave can be modeled by that of a closed-closed pipe segment of length L. In the Mach number range between 0.072 and 0.082, the frequency of the peak (f = 850 Hz) is very close to the second longitudinal acoustic mode frequency of the test section estimated by $f_{ac,2} = c_0/L$, where c_0 is the speed of sound (c_0 = 338 m/s) and L is the total length (L = 0.393 m). The oscillation frequency seems to vary slowly and linearly with the Mach number. This change takes care for the necessary phase shift needed to compensate for the change in travel time of vortical structures which is needed to obtain a phase shift equal to an integer number of 2π along the feedback loop. This phenomena has been extensively described for deep cavities[24,25] and the flute.[26,27] We will therefore call this a flute behavior.

Making a zoom between 780 Hz and 900 Hz (figure 7a) shows that the slope of the evolution for Mach number between 0.072 and 0.082 is different than the slopes for lower or higher Mach numbers. The variation of the slope of the frequency evolution can only be produced by the acoustic resonance of the test section due to a vortex shedding at that frequency. To confirm this affirmation, one has to demonstrate that the vortex shedding occurs at the second longitudinal acoustic mode frequency.

Figure 7b shows the contour of the velocity fluctuations measured by[9] with the hot wire located at 13 mm from the wall and at 37.5 mm downstream the inhibitor. There, the hot wire is on the path of the vortices shed by the inhibitor.[28] proved that the hot wire signal is mainly determined by the vortical velocity fluctuations produced by the flow and is not sensitive to the acoustics. Indeed, pulsations correspond to acoustical pressure amplitude of the order of $|p'|/p_0 = O(10^{-3})$ of the static pressure $p_0 = \rho_0 c_0^2/\gamma$ in the reservoir. When an acoustical standing wave is assumed this will correspond to acoustical velocity fluctuations (in plane waves) which are of the order of $|u'|/c_0 \simeq |p'|/\gamma p_0 = O(10^{-3})$ at the pressure nodes. For a main flow Mach number $U_0/c_0 = O(10^{-1})$, this corresponds to $|u'|/U_0 = O(10^{-2})$, which is negligible compared to the velocity fluctuations generated by the flow (for instance, vortex shedding). Therefore, the spectrum of the signal acquired with the hot wire (figure 7b) allows determination of the vortex shedding frequency. That frequency appears to correspond to the second longitudinal acoustic mode frequency (figure 7a). So, vortex shedding occurs at one of the acoustic mode frequency and excites the acoustic properties of the test section. Furthermore, the resonance modifies the vortex shedding frequency evolution (figure 7b). Without acoustic resonance, the slope of the vortex shedding frequency evolution would correspond to a constant Strouhal number. This is observed by[5] during the initial phase of the combustion. These observations prove the occurrence of a flow-acoustic coupling of the flute type in our model.

Figure 4a can also be plotted in term of Helmholtz number $He = fl/c_0$ instead of frequency f. As l and c_0 are constant, He is a non dimensional representation of the pressure fluctuation frequency. Figure 8a shows the pressure fluctuation spectrum plotted versus Mach number M_0 and Helmholtz number He. Finally, the maximum of the pressure fluctuation values are plotted versus Mach number in figure 8b. The evolution of the Helmholtz number corresponding to the maximum of the pressure fluctuations is also given in figure 8b. In such plot, the longitudinal acoustic modes of the test section characterized by $He_{ac,j} = jl/(2L)$ correspond to horizontal lines. For such test conditions, each time the excited frequency is close to an acoustic mode frequency, the pressure fluctuation level is large. The maximum is reached when it crosses the acoustic mode.

Looking at figure 8b, the maximum of the sound pressure level is observed experimentally to excite the second mode at a Mach number M_0 equal to 0.082. It is worth applying an analytical model developed on purpose and based on Rossiter's approach (equation 10) to compare the M_0-value at which the maximum of the sound pressure level is observed. The inhibitor is placed at 26 % from the end of the test section. Then, the excited mode j will be preferably

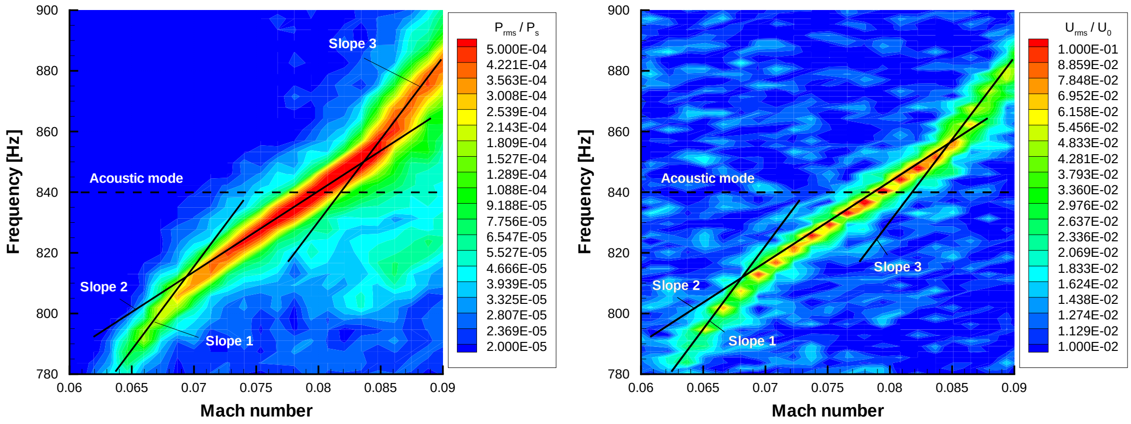

(a) Pressure fluctuations (b) Velocity fluctuations

Figure 7: Contour of pressure fluctuations (a) and velocity fluctuations between 780 and 900 Hz (b). L = 393 mm ; l = 71 mm ; d = 58 mm ; submerged nozzle.

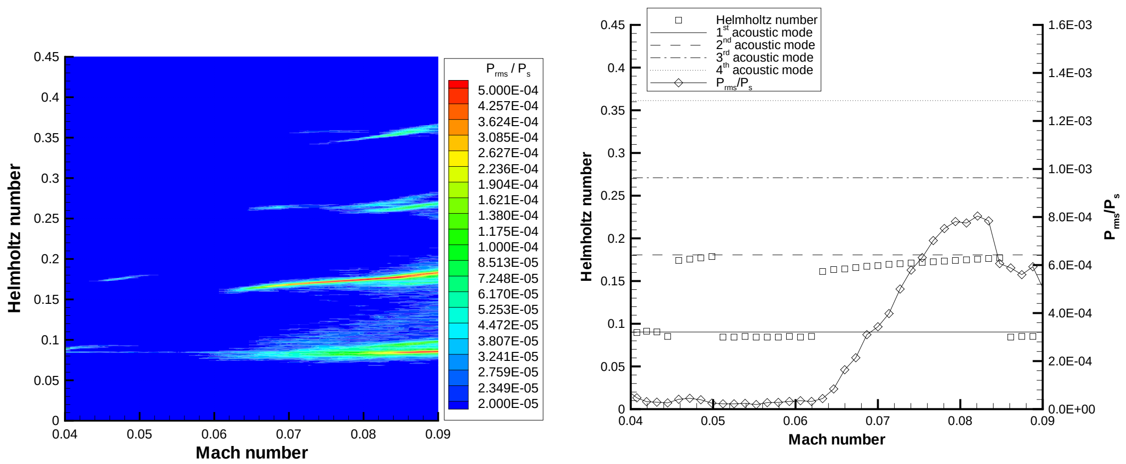

(a) (b)

Figure 8: Contours of pressure fluctuations (a) and evolution of the maximum of the pressure fluctuation, in terms of Helmholtz number and amplitude (b). L = 393 mm ; l = 71 mm ; d = 58 mm ; submerged nozzle.

the second longitudinal acoustic mode, as its acoustic pressure node is theoretically at 25 % from the test section backward end (figure 6). From equation 10:

$$M_0 = \frac{C_{vc}}{2k_v}\frac{j}{m-0.25}\frac{l}{L}\left(\frac{d}{D}\right)^2 = \left(\frac{0.68}{2*0.47}\right)\left(\frac{2}{m-0.25}\right)\left(\frac{71}{393}\right)\left(\frac{58}{76}\right)^2 = \frac{0.15}{m-0.25} \tag{12}$$

a flow-acoustic coupling is predicted to occur at a Mach number equal to 0.086 with m = 2 vortices located between the inhibitor and the nozzle. Such a finding is in good agreement with numerical simulations[29] and experimental observation obtained from PIV (Particle Image Velocimetry) measurements.[30]

6. Passive control of pressure oscillations

As explained in the previous section, the best solution for passive control of the pressure oscillations is to replace the submerged nozzle by a non integrated nozzle (without cavity). However, in practice this integration allows orientation of the nozzle through a flexible bearing to provide adaptation of the rocket trajectory during the launch. For evident practical reasons, it is then not possible to remove the integration.

The flow-acoustic feedback loop relies upon the interaction between the vortices and the nozzle. Therefore, the general idea of the passive control of pressure oscillations is to prevent the vortices to interact with the nozzle cavity. As indicated by the original analytical model developed by Anthoine *et al.*[9] and based on vortex-sound theory (relation 1), the nozzle geometry is expected to play an important role in the amplification of the sound pressure fluctuations. This has been proved experimentally[7,9] (figure 4b). So, the best solution for passive control of the pressure oscillations is to replace the submerged nozzle by a non integrated nozzle (without cavity). However, in practice this integration allows orientation of the nozzle through a flexible bearing to provide adaptation of the rocket trajectory during the launch. For evident practical reasons, the removing of the integration would involve a lot of other modifications in the operation of the launcher. So, alternative ways should be first investigated. The following solutions are proposed to achieve this goal:

- Insertion of a membrane (impermeable or permeable) in front of the cavity entrance to prevent vortex/nozzle interaction ;
- Modification of the inhibitor geometry (3D shaped, outlying) to reduce the vortex coherence ;
- Installation of a resonator (Helmholtz resonator or quarter wavelength tube) to damp the pressure oscillations.

6.1 Insertion of a membrane

The idea is to prevent the vortices to interact with the nozzle cavity while passing in front of the cavity entrance by inserting a solid membrane at the entrance of the cavity. The first membrane to be tested is completely impermeable (figure 9a) and is expected to damp completely the pressure oscillations, since the flow-acoustic coupling should disappear. In fact, the results should be similar to those obtained without cavity at the nozzle. This membrane is then the best solution for passive control of integrated nozzle. However, using a solid membrane, the integrated nozzle cannot be surrounded by propellant. The last propellant grain should be between the inhibitor and the membrane. This will result in a reduction of the performance of the launcher, since the ratio of propellant mass to inert mass is reduced.

To overcome this problem of propellant mass reduction, the next idea is to use a permeable membrane for passive control (figure 9b). That membrane presents 16 small circular holes through which the flow coming from the propellant combustion can exit the nozzle cavity. The diameter of the holes is equal to 6 mm. The motor performance should not be affected by this membrane but the vortices are still able to interact with the acoustic fluctuations induced by the cavity volume. It is however expected that this interaction will be weaker than without membrane producing smaller pressure oscillations.

(a) Impermeable membrane (b) Permeable membrane (c) Membrane in test section

Figure 9: The two membranes for passive control of pressure oscillations.

The analytical model (relation 1) is adapted for the passive control with permeable membrane to determine the attenuation factor of the pressure oscillations. The difference compared to what was done previously[9] to obtain equation 1 is that

- the cross-surface S_c of the cavity entrance is reduced to the section of the 16 holes in the permeable membrane $S_c = 4\pi D_h^2$, where D_h is the diameter of the holes in the membrane,
- the mean distance over which the vortex travels in front of the cavity entrance is reduced to the mean distance in vortex path direction over the hole cross-surface, $\pi D_h/4$.

The compressibility of the gas in the cavity volume V_c induces an acoustic fluctuation u' through the cross-surface S_c of the holes of the membrane such that from mass conservation it follows:

$$\rho_0 u' S_c \simeq \frac{V_c}{c_0^2}\frac{dp'}{dt} \tag{13}$$

where we made use of the fact that the cavity is small compared to the acoustical wave length ($\lambda \sim L$). The acoustic velocity u' is the component of $\boldsymbol{u}'$ normal to the vortex path taken positive when it is directed from the cavity towards the main flow. Assuming a harmonically oscillating acoustic field ($u' = |u'|e^{i2\pi ft}$ and $p' = |p'|e^{i2\pi ft}$, where f is the acoustic frequency), one can write:

$$|u'| = \frac{2\pi f V_c}{\rho_0 c_0^2 S_c}|p'| \tag{14}$$

At low Mach numbers as occurring here, the time average acoustic power $\mathcal{P}$ is given by the vortex-sound theory developed by[31] and[32]:

$$\mathcal{P} = -\rho_0 \langle \int_V (\boldsymbol{\omega} \times \boldsymbol{v}) \cdot \boldsymbol{u}' dV \rangle \tag{15}$$

where V is the source volume (where $\boldsymbol{\omega} \neq 0$). The brackets indicate the averaging over one period of a steady oscillation. The maximum of acoustic power is then expressed by:

$$\mathcal{P}_{max} \sim \rho_0 |\boldsymbol{v}||\boldsymbol{u}'| \int_V |\omega| dV \sim \rho_0 |\boldsymbol{v}||\boldsymbol{u}'|(\pi D \Gamma) \sim \rho_0 \frac{U_0}{2} \frac{2\pi f V_c}{\rho_0 c_0^2 S_c}|p'|\pi D \frac{U_0^2}{4f} \tag{16}$$

where $|\boldsymbol{v}|$ is approximated by half the mean flow velocity $U_0/2$, $|\boldsymbol{u}'|$ is given by equation 14 and the circulation Γ is given by:

$$\Gamma \sim l_v \frac{U_0}{2} \sim \frac{U_0^2}{4f} \tag{17}$$

where l_v is the distance on which the vortex accumulates the vorticity, assumed to be equal to the distance between two successive vortices ($l_v \sim U_0/(2f)$).

However, vortices produce sound only when passing in front of the holes of the membrane. We do expect that for maximum pulsation the vortex will pass along the cavity at the time corresponding to the maximum power generation. A weighting coefficient has to be introduced in equation 16 to take into account the time fraction T_c during which the vortex travels in front of the cavity entrance compared to the vortex shedding period $T = 1/f$. Another weighting coefficient has to take into account the portion of the vortex ring passing in front of the holes, since the holes cross-surface is smaller than the vortex ring surface. The coefficients are equal to

$$\frac{T_c}{T}\frac{A_{holes}}{A_{vortex}} = \frac{2f\pi D_h}{4U_0}\frac{4\pi D_h^2}{\pi D D_h} = \frac{2\pi f D_h^2}{D U_0} \tag{18}$$

Then, combining equations 16 and 18 and using $S_c = 4\pi D_h^2$, the generated acoustical power becomes, after simplification:

$$\mathcal{P} \sim \frac{\pi^2}{8} M_0^2 f V_c |p'| \tag{19}$$

On the other hand, assuming that the acoustic losses are dominated by the radiation at the nozzle, the acoustic power is the work of the fluctuating pressure per unit time which can be expressed as:

$$\mathcal{P} = \langle p'u' \rangle \frac{\pi D^2}{4} \sim \frac{|p'|^2}{2}\frac{\pi D^2}{4}\frac{1}{Z_n} \qquad \text{where} \qquad Z_n = \left(\frac{p'}{u'}\right)_{nozzle} \tag{20}$$

This impedance is expected to be reasonably described by a quasi-stationary model.[33] The key idea is to calculate the fluctuations of the pressure at the nozzle inlet by means of a subsonic flow model, and to consider that the Mach number is constant in spite of the pressure unsteadiness:

$$dM_0 = 0 \qquad \rightarrow \qquad d\left(\frac{u}{c_0}\right) = 0 \qquad \rightarrow \qquad \frac{u'}{u} = \frac{c_0'}{c_0} \tag{21}$$

Knowing that $c_0 = \sqrt{\gamma p/\rho}$ and assuming isentropic evolution $p\rho^{-\gamma} = cst$, one gets:

$$\frac{u'}{u} = \frac{c_0'}{c_0} = \frac{1}{2}\frac{(p/\rho)'}{(p/\rho)} = \frac{\gamma - 1}{2\gamma}\frac{p'}{p} \tag{22}$$

or, with $\gamma p = \rho c_0^2$,

$$\rho c_0 u' = M_0 \frac{\gamma - 1}{2} p' \tag{23}$$

Hence the impedance of the nozzle reduces to:

$$Z_n = \frac{2\rho c_0}{M_0(\gamma - 1)} \tag{24}$$

Therefore, when equations 19, 20 and 24 are combined, the pressure oscillation level is given by:

$$\frac{|p'|}{p_0} \sim \frac{\pi^2\gamma}{4(\gamma - 1)} jM_0 \frac{V_c}{V_{tot}} \qquad \text{where} \qquad V_{tot} = \frac{\pi D^2}{4} L \tag{25}$$

This last equation should be compared to equation 1. When resonance occurs, the sound pressure level is still a linear function of the Mach number, the excited mode number and the nozzle cavity volume. A weak point in this model is that it is assumed that the vortex trajectory remains independent of the geometry of the cavity inlet (presence or not of the permeable membrane).

The attenuation factor of the pressure oscillations can then be expressed by comparing equations 1 and 25. When using the permeable membrane shown in figure 9b, the attenuation is given by:

$$\frac{|p'_{control}|}{|p'_{no\ control}|} \sim \frac{\pi}{4} \tag{26}$$

Experiments are also performed in the axially injected cold flow model (figure 3a), with and without passive control. The two membranes are made of brass and have a thickness of 2 mm. They have the same length than the last segment of the axial model. So, this last segment can be replaced by one of the passive control membrane keeping the total length L constant, as shown in figure 9c. This figure has to be compared to figure 3a. To guarantee zero pressure balance on both sides of the membrane, a slit of 1.5 mm exists between the membrane and the nozzle head.

Pressure fluctuations are measured for an inhibitor with orifice diameter of d = 0.058 m placed at a distance l = 0.071 m from the head of the submerged nozzle. The exact value of the length L of the test section depends on the nozzle geometry and is around L = 0.38 m. The results are provided in figure 10b for the impermeable membrane and in figure 10c for the permeable membrane and can be compared to submerged nozzle without membrane (figure 10a) and to the nozzle without cavity (figure 10d). The last result has been presented earlier.[9]

The evolution of the Helmholtz number is similar for the submerged nozzle without passive control and the same nozzle with permeable membrane. This evolution is different for the two other test cases (impermeable membrane and without cavity). That means that the vortex shedding does excite the second longitudinal acoustic mode within the same Mach number range for the two first cases, but not for the two latest. The maximum of sound pressure levels that corresponds to a coupling on the second acoustic mode appears at M_0 = 0.08. But the amplitude of the maximum resonance is influenced by the use of passive control.

The maximum of the pressure fluctuation is plotted versus Mach number for the different test cases in figure 11. Without cavity, the pressure fluctuation levels remain similar whatever the Mach number indicating that vortex-acoustical coupling has disappeared. In such condition, the pressure level is reduced by a factor above 10. As expected, the passive control with impermeable membrane produces the same pressure oscillations than when the cavity is not present, so a reduction by a factor above 10. This proves again that the pressure oscillations are induced by the presence of the cavity, through a coupling between the acoustic fluctuations induced by the cavity volume and the vortices traveling in front of the cavity entrance, as already explained through the analytical model.

However, using an impermeable membrane, the integrated nozzle cannot be surrounded by propellant, which results in a reduction of the performance of the launcher, as explained before. To overcome this problem of propellant mass reduction, the passive control of the pressure oscillations is then obtained using a permeable membrane. Of course the attenuation of the pressure oscillations is less than without cavity or with the impermeable membrane. Still, the permeable membrane allows reducing the pressure oscillations by a factor 1.5 compared to the case without passive control (attenuation factor of 0.67). This attenuation is close to the analytical model prediction ($\pi/4$) given by relation 26.

6.2 Modification of the inhibitor geometry

Pressure fluctuations are first obtained for inhibitors of three different internal diameters (d = 58, 62 and 68 mm, corresponding to inhibitor heights equal to 9, 7 and 4 mmm, respectively), placed at 71 mm from the head of the submerged nozzle. Figure 12 shows the evolution of the maximum of the pressure fluctuation, in terms of Helmholtz number and amplitude, versus the Mach number M_0 for the three inhibitors. The Mach number M_0 is computed upstream the inhibitor and does not take into account the inhibitor internal diameter or height. Following the excitation of an acoustic mode, resonance appears for higher Mach number when the internal diameter d of the inhibitor increases,

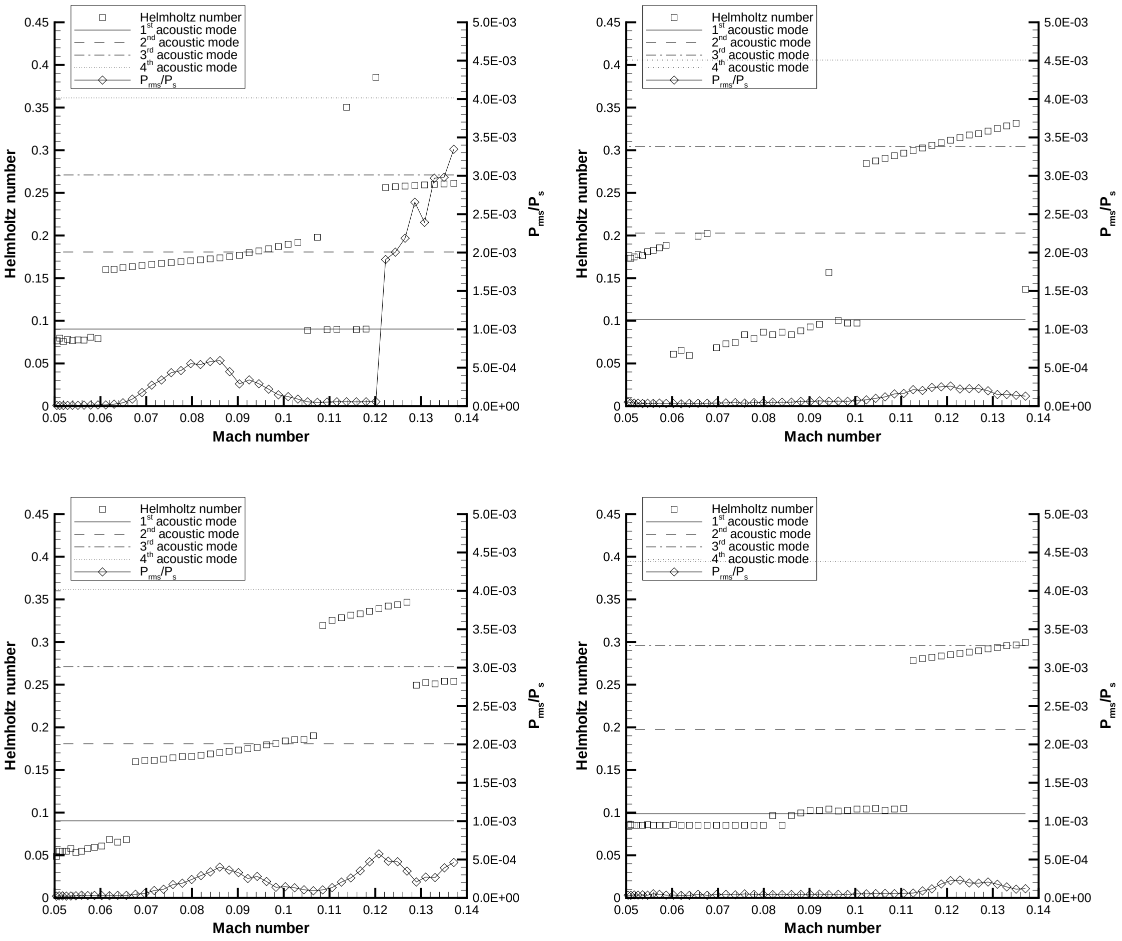

(c) Submerged nozzle with permeable membrane

(d) Nozzle without cavity[9]

Figure 10: Evolution of the maximum pressure fluctuation, in terms of Helmholtz number and amplitude, for submerged nozzle without passive control (submerged nozzle), submerged nozzle with permeable membrane, submerged nozzle with impermeable membrane and nozzle without cavity. l = 0.071 m ; d = 0.058 m.

so when h decreases. Since the ratio C_{vc}/k_v increases (flow acceleration), the Mach number to get resonance should augment in accordance with equation 10.

The effect of an increase of the inhibitor diameter on the Mach number is similar to a raise of the inhibitor-nozzle distance, as indicated by equation 10. Indeed, if we want to keep resonance on the same acoustic mode and for the same number of vortices (same values of i and m), the Mach number M_0 has to be increased when augmenting the inhibitor-nozzle distance l or when diminishing the inhibitor height h. This justifies the conclusion that the important inhibitor parameter would be the ratio l/h.

Without inhibitor, the level of pressure fluctuation remains constant and very low ($P_{rms}/P_s = 10^{-4}$) whatever the Mach number (figure 12d. When the inhibitor is far away or when the inhibitor height is small ($l/h = 18$), the pressure level variations are similar to those without inhibitor, meaning that there is no flow-acoustic coupling since the inhibitor operates like an isolated obstacle, except at very high Mach number for which the vortices can still reach the nozzle. When reducing the l/h ratio, peaks in pressure evolution appear meaning that resonance is occurring. For $l/h = 10$, the level is amplified to $P_{rms}/P_s = 10^{-3}$. The maximum is reached for $l/h = 8$ ($P_{rms}/P_s = 3.5 \times 10^{-3}$). Therefore, approaching the inhibitor closer to the nozzle or increasing the inhibitor height has the effect of raising the sound resonance level. That higher resonance comes from a stronger vortex nozzle interaction resulting from more powerful vortices impinging on the nozzle. Indeed, in axial injected flow, the vortices become weaker as they are traveling downstream of the shedding point.[30] Thus, approaching the inhibitor closer to the nozzle has the effect to reduce the vortex transport distance, while increasing the inhibitor height has the effect to decrease the vortex transport time (increasing flow velocity). In both cases, the vortices are stronger when interacting with the nozzle leading to

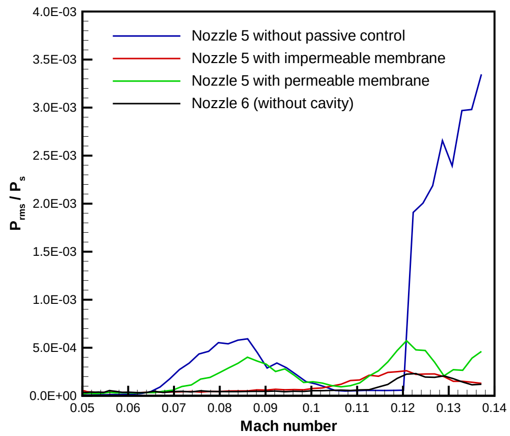

Figure 11: Evolution of the maximum pressure fluctuations for the submerged nozzle without passive control, the submerged nozzle with permeable membrane, the submerged nozzle with impermeable membrane and the nozzle without cavity. l = 0.071 m ; d = 0.058 m.

higher pressure levels. Of course, there should be an optimum value of the l/h ratio below which the pressure levels lessen. At the limit, when the ratio tends to zero (l = 0), the vortices have no time to be generated and flow-acoustic coupling does not occur.

All the previous tests are done considering inhibitors with a circular opening coaxial with the segments (axisymmetric shape). The pressure fluctuations are then also measured for 3D-shaped inhibitors placed at a distance l = 0.071 m from the head of the submerged nozzle. The inhibitors designed for this purpose are plotted in figure 13. Figure 13a shows an inhibitor of diameter d = 58 mm with outlying opening (center shifted by 5.5 mm). The second inhibitor (figure 13b) has an axisymmetric opening ($d = 58\,mm$) but randomly drilled at five locations. The last inhibitor has a crenel-shaped opening section ($d = 58\,mm$) made of seven crenel cuts (figure 13c).

Figure 14 shows the evolution of the maximum of the pressure fluctuations, in terms of Helmholtz number and amplitude, versus the Mach number for the 3D-shaped inhibitors. The nominal case (axisymmetric inhibitor with d = 58 mm) is shown in figure 14d.

With the inhibitor with outlying opening, the level of pressure fluctuations lessens and both the frequency and pressure level variations are similar to those obtained with d = 68 mm (figure 12c). The height h of that inhibitor varies from 3.5 mm to 14.5 mm, but has the same influence on the frequency and pressure levels than decreasing the inhibitor height in the complete perimeter, as happens for the inhibitor of 68 mm, where the height h is constant and equal to $4\,mm$.

The evolution of the maximum of the pressure fluctuations for the inhibitor with axisymmetric opening but randomly drilled is similar to that obtained with d = 62 mm (figure 12b). In both cases, the cross-section of the inhibitor is increased, as indicated in table 3, which results in a shift of the Mach number range compared to the nominal case (figure 14d). This shift was already found analytically in relation 10. From relation 1, the pressure oscillations are linearly proportional to the Mach number. Therefore, a shift of the Mach number should be associated to a proportional increase of the pressure oscillations. However, the pressure level amplitude associated to the randomly drilled inhibitor is slightly decreased. Taking into account the expected increase due to the Mach number shift, the effective reduction of the pressure oscillations is equal to 25%. So, the asymmetric shape of the drilled inhibitor allows to reduce the pressure level amplitude.

Regarding the crenel-shaped inhibitor with the same inner diameter than the nominal case, the conclusions are similar than for the drilled inhibitor. The excitation remains on the second acoustic mode but for a higher Mach number due to the increase of the cross-section (table 3) compared to the nominal case. This shift of the Mach number is again proportional to the increase of the cross-section. Taking into account the expected increase of pressure oscillations level due to the Mach number shift (relation 1), the effective reduction of the pressure level is equal to 33%. The cross-section of the crenel-shaped inhibitor is very similar to the one obtained with the inhibitor of d = 62 mm (figure 12b). However, for the axisymmetric inhibitor (d = 62 mm), the increase of the pressure level compared to the nominal case is equal to 67%, while the expected augmentation of pressure oscillations due to the Mach number shift associated to the cross-section increase (relation 1) is 29%. Therefore, for the same cross-section corresponding to the excitation of the same acoustic mode at the same Mach number (M_0 = 0.11), the axisymmetric inhibitor provides a net increase

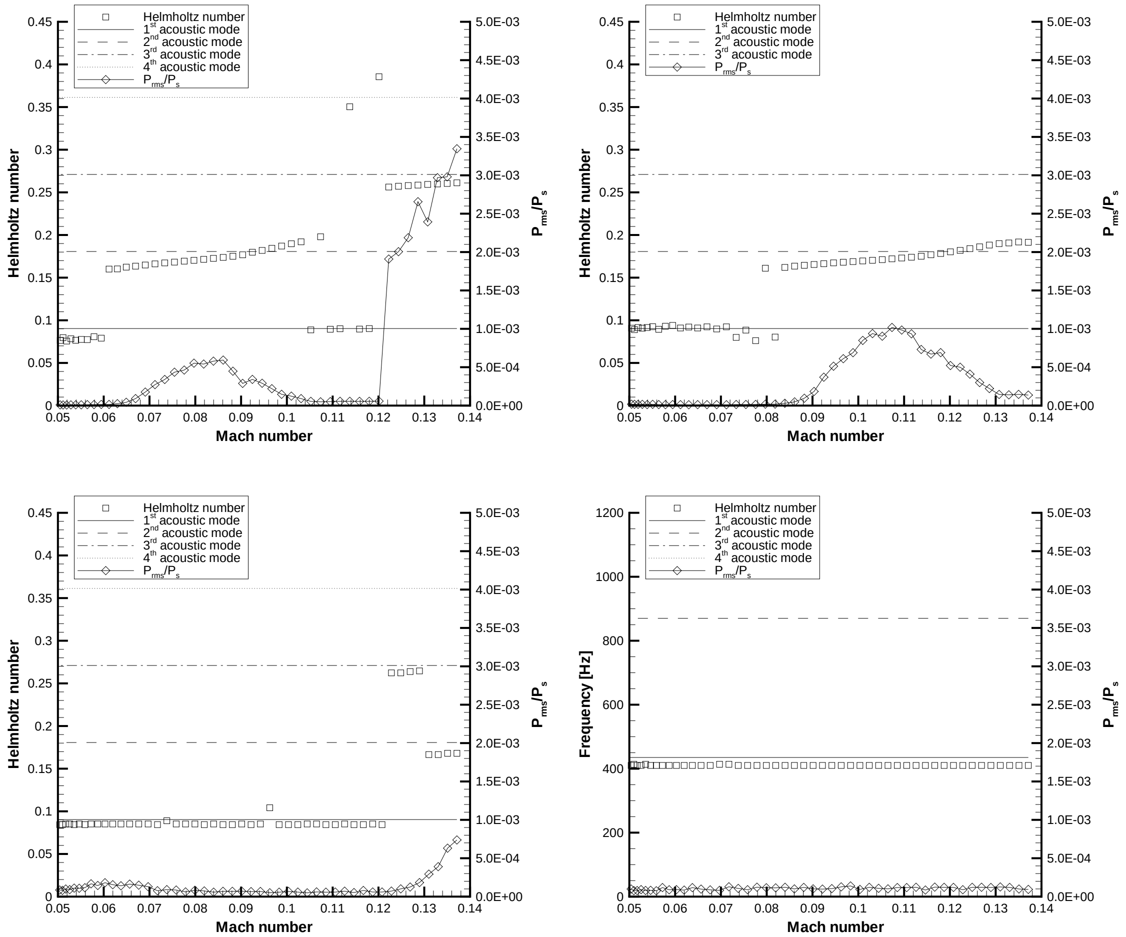

(c) d = 68 mm, l/h = 18 (d) Without inhibitor

Figure 12: Evolution of the maximum of the pressure fluctuation, in terms of Helmholtz number and amplitude. L = 393 mm ; l = 71 mm ; submerged nozzle.

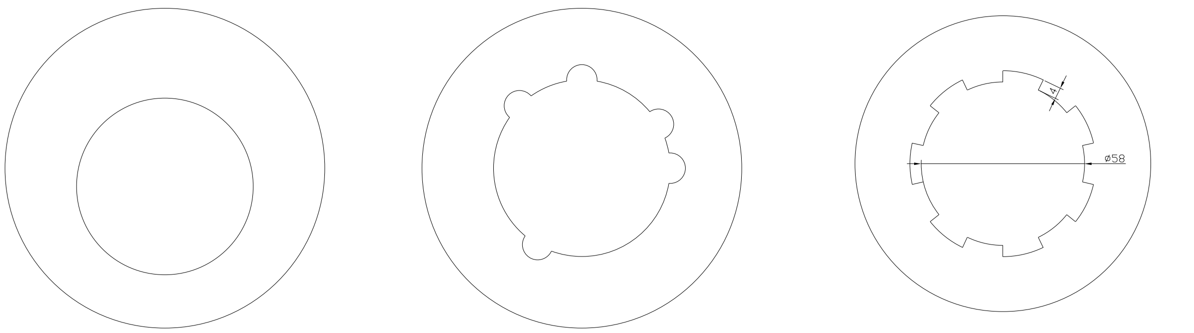

(a) Outlying opening (b) Axisymmetric opening but randomly drilled (c) Crenel-shaped opening (same diameter)

Figure 13: 3D-shaped inhibitors.

of pressure level by 37%, while the asymmetric inhibitor (crenel-shaped) provides a net reduction of 33%.

These results also confirmed that, as expected from relation 10, the increase of the cross-section of the inhibitor is associated to a proportional shift of the Mach number, as plotted in figure 15. The Mach number that crosses the second acoutic mode versus the opening area follows a linear evolution and, therefore, if the opening area of the inhibitor is

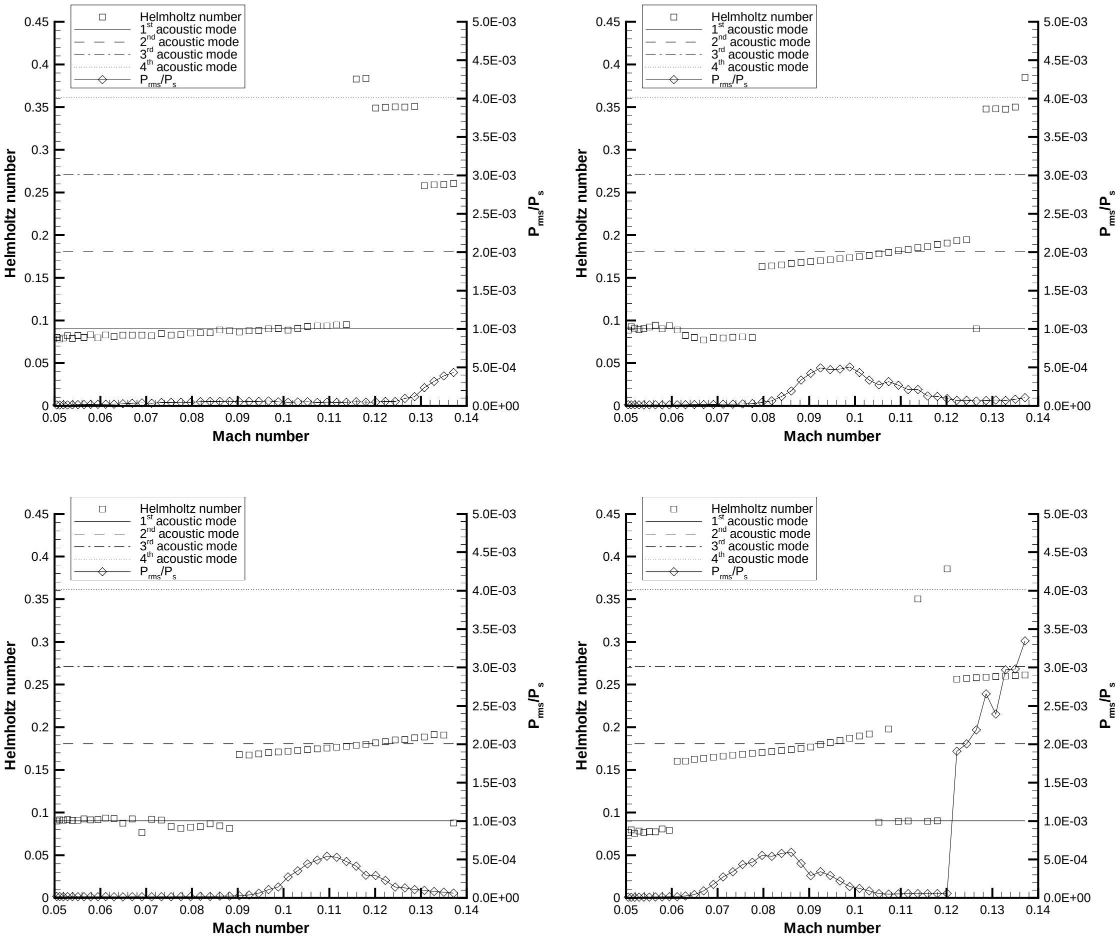

(c) Crenel-shaped opening (d) Nominal case

Figure 14: Evolution of the maximum of the pressure fluctuation, in terms of Helmholtz number and amplitude for the 3D-shaped inhibitors. Submerged nozzle ; l = 0.071 m ; d = 0.058 m.

higher than $3.6 \times 10^{-3}\mathrm{m}^2$, the second longitudinal mode of the present setup is not excited.

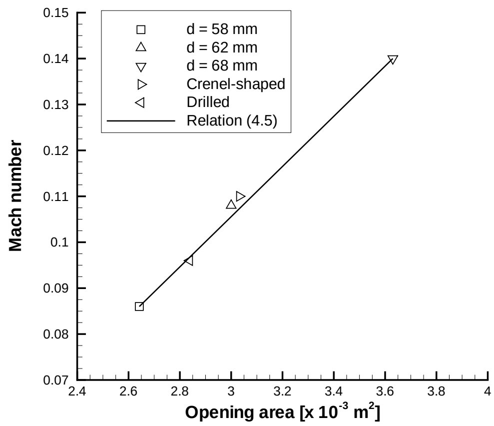

Figure 15: Evolution of the Mach number that crosses the second acoustic mode versus opening area of different inhibitors.

As conclusion, the asymmetry of the inhibitor provides a promising way of reducing the pressure oscillations.

Inhibitor	Opening area [$\times 10^{-3}$m^2]	ratio	Mach number	Maximum P_{rms}/P_s [$\times 10^{-4}$]	ratio	Net increase (+) or reduction (-)
d = 58 mm	2.642	1	0.085	6	1	0
d = 62 mm	3.019	1.14	0.11	10	1.67	+37%
Drilled	2.838	1.07	0.095	5	0.83	−25%
Crenel-shaped	3.032	1.14	0.11	5.2	0.87	−33%

Table 3: Opening area of the inhibitors (the two first are axisymmetric ; the two last are asymmetric) and corresponding Mach number for excitation of the second acoustic mode.

These results have also been observed recently by ONERA (under a CNES supported activity).[34] performed a parametric investigation with different asymmetric inhibitor shapes, including crenel-shaped inhibitors and showed that all of them provide a reduction of the pressure oscillation levels. However, it was not possible to determine experimentally the effect of the different parameters (type of asymmetry, number and height of the crenel cuts, ...).

6.3 Installation of a resonator

Resonators are acoustical elements used to attenuate the sound at narrow band frequencies both in ducts and tubes. A simple resonator comprises a cavity enclosing a mass of air, with a narrow opening to the outside. In this way, the mass of air effectively acts as a “spring” at the resonant frequency of the cavity and under those conditions absorbs appreciable sound energy exciting the resonance. Two types of resonators were designed and tested in the experimental set-up: the quarter wavelength tube and the Helmholtz resonator.

6.3.1 Quarter wavelength tube

The quarter wavelength tube is a tube closed at one of its extremity and connected through its other extremity to the test section, in which pressure oscillations need to be damped, as sketched in figure 16. The frequency at which the quarter wavelength tube could act as a damper is controlled by its length L_t. The maximum attenuation is achieved when the cross-section of the quarter wavelength tube matches that of the test section to which it is connected, which is technically impossible in our case. In the present set-up, the test section has a diameter of 0.076 m and the diameter of the quarter wavelength tube cannot be larger than 0.01 m.

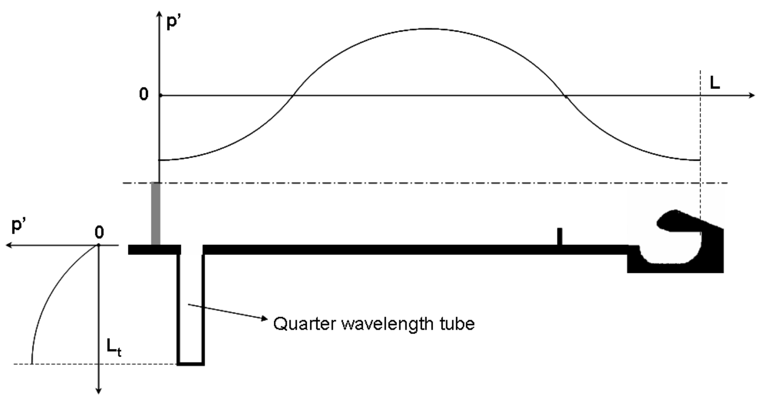

Figure 16: Sketch of the quarter wavelength tube.

As its name indicates, the quarter wavelength tube has a length that equals to the wavelength of the mode to be attenuated divided by 4. The total distance that the acoustic wave travels within the resonator is then half a wavelength. So, the pressure pulse fed into the quarter wave tube is reflected back from the end of the tube to the test section half a cycle later. At this time, the oscillating pressure in the test section is in opposite phase to the reflected pulse, so that a rarefaction now exists at the tube entrance. When the reflected pressure pulse meets the rarefaction, attenuation of the oscillating component of the test section is obtained.[35] This resonator is quite insensitive to its position as long as it is in the pressure anti-node and its construction has a low cost. The only drawback is that it has a narrow frequency range of effectiveness and it is very sensitive to the manufacture length.

The fundamental resonant frequency of a quarter wavelength tube is given by equation 27,

$$f_r = \frac{c_0}{4\,L_t} \tag{27}$$

where c_0 is the speed of sound and L_t is the length of the resonator.

Two resonators of that type are tested to damp the pressure oscillations obtained for the nominal configuration (l = 0.071 m, d = 0.058 m, L = 0.393 m, submerged nozzle). One of them is designed to attenuate the second longitudinal acoustic mode observed at $M_0 = 0.08$, while the second one is designed to damp the third acoustic mode at $M_0 = 0.14$. The corresponding frequency and wavelength tube length are 873 Hz and 0.098 m for the second mode resonator and 1309 Hz and 0.066 m for the third mode resonator.

Figure 17a shows the pressure fluctuation amplitude and Helmholtz number in function of the Mach number when the quarter wavelength tube designed to damp the second acoustic mode is applied. Figure 17b provides the results when using the second quarter wavelength tube designed to attenuate the third acoustic mode. The results plotted in these two figures have to be compared to figure 14d. The comparison of the pressure fluctuation levels for the three cases is also shown in figure 18. Both tubes reduce the amplitude of the pressure fluctuations when the Helmholtz number matches the acoustic mode for which they have been designed: in the interval $0.08 < M_0 < 0.09$ for the second mode (figure 17a) and when $M_0 > 0.12$ for the third mode (figure 17b). The attenuation of the third mode proves to be more effective in the present range of Mach number. As it was shown by,[36] the resonators have to be designed and built for the optimun length in order to maximize the acoustic damping of the longitudinal mode frequency, and a small deviation is enough to decrease drastically the efficiency, which can explain the lower efficiency of the resonator for the second mode. Another explanation is the too small ratio between the resonator cross-section and the test section cross-section. As said before, that ratio should be as close as possible to 1, which was not technically possible here (the ratio for the present test is equal to 0.02).

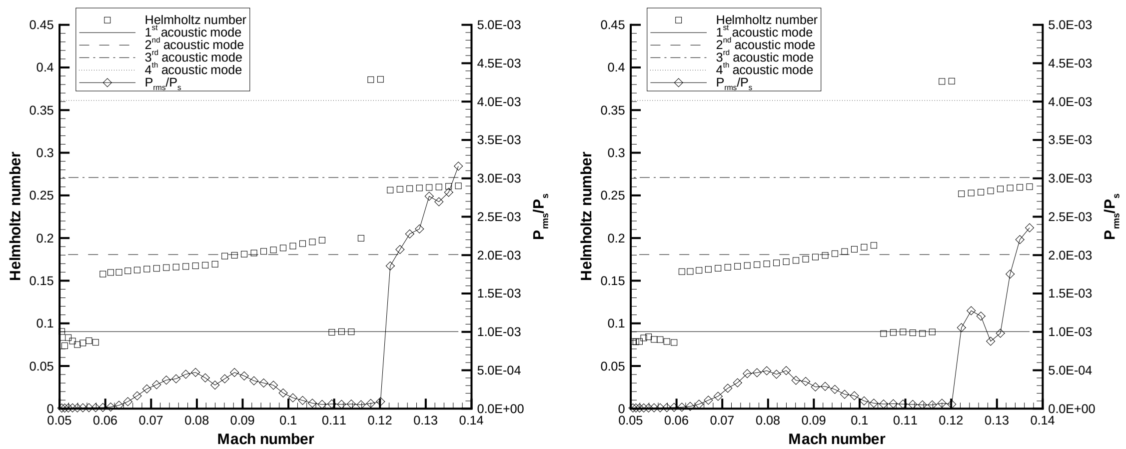

(a) Quarter wavelength tube, 2^{nd} mode

(b) Quarter wavelength tube, 3^{rd} mode

Figure 17: Evolution of the maximum of the pressure fluctuation, in terms of Helmholtz number and amplitude, with two different quarter wavelength tubes used as resonators. Submerged nozzle ; l = 0.071 m ; d = 0.058 m ; L = 0.393 m.

6.3.2 Helmholtz resonator

The Helmholtz resonator is an acoustic filter element. It is effectively a mass on a spring (single degree of freedom system), where the large volume V is the spring and the volume of air in the neck is the mass. This analogy is plotted in figure 19 and equations 28 and 29 give the equivalent values of mass and stiffness, respectively:

$$m = \rho_0 S\, l_N \tag{28}$$

$$K = \frac{S^2 \rho_0 c^2}{V} \tag{29}$$

Taking into account that in a spring-mass system the natural period of the oscillation is established from $\omega_n \tau = 2\pi$, or

$$\tau = 2\pi \sqrt{\frac{m}{K}} \tag{30}$$

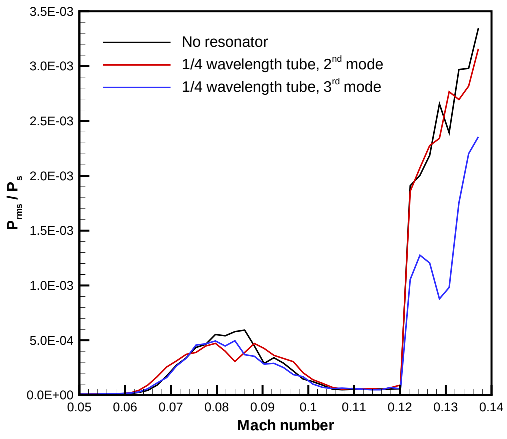

Figure 18: Evolution of the maximum amplitude of the pressure fluctuation with two different quarter wavelength tubes used as resonators. Submerged nozzle ; l = 0.071 m ; d = 0.058 m ; L = 0.393 m. Submerged nozzle ; l = 0.071 m ; d = 0.058 m ; L = 0.393 m.

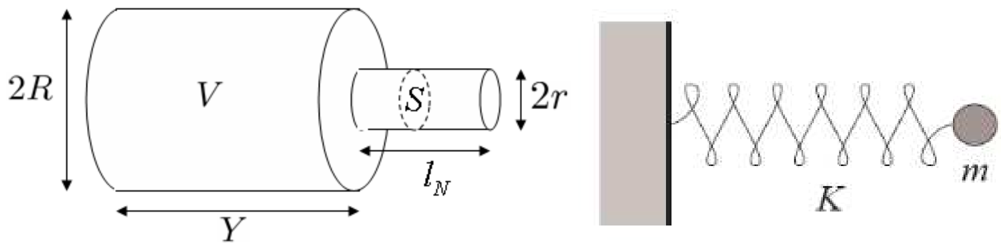

Figure 19: Main design parameters of the Helmholtz resonator and its analogy to the spring-mass system

the natural frequency f_n results

$$f_n = \frac{1}{\tau} = \frac{1}{2\pi}\sqrt{\frac{K}{m}} \tag{31}$$

Replacing K and m from equations 28 and 29 in equation 31, the resonant frequency of the Helmholtz resonator is given by:

$$f_r = \frac{c}{2\pi}\sqrt{\frac{S}{V(l_N + 2\delta)}} \tag{32}$$

The correction factor δ depends on the radius of the neck, r. It has been found in literature that when the Helmholtz resonator is mounted as a a branch[37] the correction factor is:

$$2\delta = 1.7r \tag{33}$$

Relation 32 has three degrees of freedom (V, S and l_N). However, there are several limitations coming from the experimental set-up which have to be respected during the design process: the radius of the neck r must be lower than 0.0065 m and the length l_N bigger than 0.03 m. By means of these two values, of equation 32 and knowing the fundamental resonance frequencies of the nominal configuration, the volume V of the resonator can be determined and is indicated in table 4.

Acoustic mode	Frequency [Hz]	V [$\times 10^{-6}$m^3]
2^{nd}	873	12.4
3^{rd}	1309	5.5

Table 4: Helmholtz resonator.

In order to determine the radius R and the length Y out of the target volume V, two more design conditions have to be respected:

$$R > r \qquad\qquad Y > 2r$$

From these conditions, only the resonator attenuating the second acoustic mode can be designed. Table 5 summarizes the main dimensions of this resonator.

Acoustic mode	Frequency [Hz]	l_N [m]	r [m]	V [m^3]	Y [m]	R [m]
2^{nd}	873	0.03	0.0065	12.4×10^{-6}	0.026	0.0125

Table 5: Dimensions of Helmholtz resonator for the attenuation of the second acoustic mode frequency

The transmission coefficient of this resonator can be calculated using equation 34,[37] where the viscosity losses are neglected, which means that there is no net dissipation of energy from the pipe into the resonator.

$$\alpha_t = \cfrac{1}{1 + \cfrac{c^2}{4S^2\left(2\pi f_r \cfrac{l_N + 2\delta}{S} - \cfrac{c^2}{2\pi f_r V}\right)}} \tag{34}$$

This transmission coefficient becomes zero at the resonance frequency of the Helmholtz resonator $f_r = f_0 = \frac{c}{2\pi}\sqrt{\frac{S}{(l_N+2\delta)V}}$, as plotted in figure 20a. At this frequency large velocity amplitudes exist in the neck of the resonator, and all acoustic energy transmitted into the resonator cavity from the incident wave is returned to the main pipe, with such a phase relationship as to be reflected back towards the source.

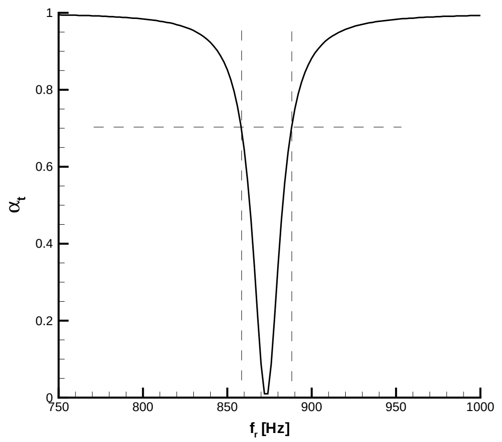

(a) Attenuation coefficient

(b) Picture

Figure 20: Attenuation coefficient and picture of the Helmholtz resonator designed for the second acoustic mode

With a modification of the design parameters l_N, S and V, the attenuation curve produced by the resonator can be wider for the same resonance frequency, but with the disadvantages of higher transmission coefficient, which means that the resonator attenuates a wider range of frequencies but less effectively.

The resonator presented in figure 20b is tested with the nominal configuration. The evolution of the pressure fluctuation amplitude and Helmholtz number in function of the Mach number is presented in figure 21. This figure has to be compared to figure 14d. At the frequency of the second acoustic mode, the maximum pressure fluctuations are attenuated by a factor of 2. However, even though the attenuation is good, the range of frequency where the Helmholtz resonator is effective is very narrow. As plotted in figure 20a, an attenuation of at least 30% is obtained between 860 Hz and 890 Hz, which corresponds to a frequency bandwidth of 30 Hz. Looking at figure 7b, the evolution of the frequency with Mach number during the acoustic coupling is approximated by line called “slope 2” for which the slope is 3000 Hz/Mach. Therefore, a frequency bandwidth of 30 Hz corresponds to a Mach range of 0.01. This is fully coherent with the results of figure 21 where the Helmholtz resonator proves to be efficient in the Mach number range between 0.08 and 0.09. As it has been already explained, this frequency bandwidth where the resonator is effective can be modified by changing the cavity and the neck dimensions. This can be improved in future designs, where some constraints presented in the present experimental set-up can be removed, like the maximum radius and the minimum length of the neck.

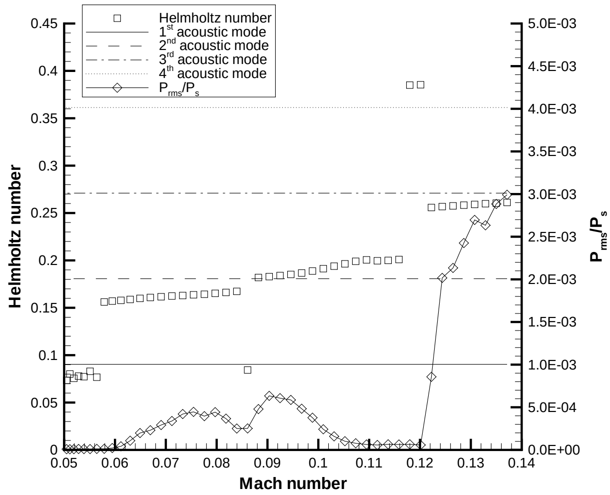

Figure 21: Evolution of the maximum of the pressure fluctuation, in terms of Helmholtz number and amplitude, with the Helmholtz resonator. Submerged nozzle ; l = 0.071 m ; d = 0.058 m ; L = 0.393 m.

Finally, if we compare the pressure fluctuation obtained with the quarter wavelength tube (designed for the second mode) and the Helmholtz resonator (figure 22), the attenuation factor is quite similar. The Helmholtz resonator gives slightly lower values of the pressure amplitude at the Mach number that crosses the second mode ($0.084 < M < 0.086$) but they are higher between $0.09 < M < 0.1$, even higher than when no resonator is used. It looks like the pressure fluctuation response with the Helmholtz resonator has shifted to higher Mach numbers. This behaviour of the pressure fluctuations with the Helmholtz resonator should be further studied under different flow conditions and with different designs of the resonator itself. This task has to be considered as crucial in future projects if this way of passive control of pressure oscillations is selected.

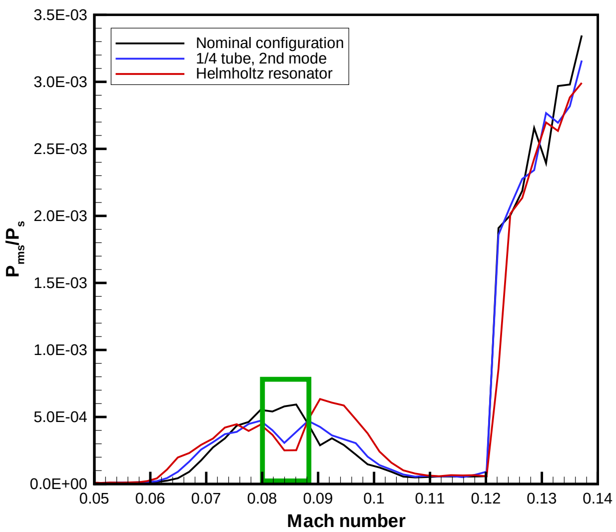

Figure 22: Evolution of the maximum amplitude of the pressure fluctuation using either a Helmholtz resonator or a quarter wavelength tube. Submerged nozzle ; l = 0.071 m ; d = 0.058 m ; L = 0.393 m.

7. Conclusions

The present research is an experimental study of aeroacoustic phenomena occurring in large solid rocket motors (SRM). The emphasis is given to aeroacoustic instabilities that may lead to pressure and thrust oscillations which reduce the rocket motor performance and could damage the payload. In previous work, original analytical models, in particular based on vortex-sound theory, cold flow experiments and numerical simulations pointed out the parameters controlling the flow-acoustic coupling and the effect of the nozzle design on sound production. The conclusions stated that flow–acoustic coupling is mainly observed for nozzles including cavity. The nozzle geometry has an effect on the pressure oscillations through a coupling between the acoustic fluctuations induced by the cavity volume and the vortices travelling in front of the cavity entrance. When resonance occurs, the sound pressure level increases linearly with the chamber Mach number, the frequency and the cavity volume.

The aim of the present research consisted to propose passive control of the pressure oscillations. Flow-acoustic coupling is only observed for nozzles including cavity and the cavity volume is playing an important role in the amplification of the pressure oscillations. The modification of the nozzle geometry can reduce by 10 the oscillations (when the cavity is completely removed). An impermeable membrane in front of the cavity gives the same result than that of a nozzle without cavity while a permeable membrane (with holes to allow for combustion gas to pass through) allows a reduction by a factor 1.5. Regarding the 3D-shaped inhibitors, they show a good attenuation of the pressure fluctuation, especially when the opening cross-section is increased. This increase results in a shift of the Mach number associated to excitation. For inhibitor cross-section larger than $3.6 \times 10^{-3}\text{m}^2$ (at model scale), the second longitudinal mode is not excited anymore. For a similar cross-section, the asymmetric inhibitor (crenel-shaped) provides a net reduction of 33% compared to an axisymmetric inhibitor. So, the asymmetry of the inhibitor provides a promising way of reducing the pressure oscillations. Finally, two types of resonators are designed and tested to damp the pressure oscillations in the model. Both the quarter wavelength tubes and the Helmholtz resonator show attenuation of the pressure oscillations but with a lower effect than the 3D-shaped inhibitors. However, their design can be optimized in order to maximize the acoustic damping.

8. Acknowledgment

This research has been supported by the European Space Agency through the ARTA program, within the ESA contract number 19581/06/F/DC. The authors would like to thank Dr. M.C. Contino and Dr. J. Steelant, both from ESA, for their support to the VKI research activities.

References

[1] Lovine, R. L. and Waugh, R. C., “Standard stability prediction method for solid rocket motors,” CPIA Publication 273, 1975.

[2] Brown, R. S., Dunlap, R., Young, S. W., and Waugh, R. C., “Vortex shedding as a source of acoustic energy in segmented solid rockets,” *Journal of Spacecraft*, Vol. 18, No. 4, 1981, pp. 312–319.

[3] Mason, D. R., Folkman, S. L., and Behring, M., “Thrust oscillations of the space shuttle solid rocket booster motor during static tests,” AIAA Paper 79–1138, 1979.

[4] Blomshield, F. S. and Mathes, H. B., “Pressure oscillations in post–challenger space shuttle redesigned solid rocket motors,” *Journal of Propulsion and Power*, Vol. 9, No. 2, 1993, pp. 217–221.

[5] Dotson, K. W., Koshigoe, S., and Pace, K. K., “Vortex shedding in a large solid rocket motor without inhibitors at the segmented interfaces,” *Journal of Propulsion and Power*, Vol. 13, No. 2, 1997, pp. 197–206.

[6] Scippa, S., Pascal, P., and Zanier, F., “Ariane–5 MPS: Chamber pressure oscillations full scale firings results analysis and further studies,” AIAA Paper 94–3068, 1994.

[7] Anthoine, J., *Experimental and numerical study of aeroacoustic phenomena in large solid propellant boosters*, Ph.D. thesis, Université Libre de Bruxelles, October 2000.

[8] Guéry, J.-F., Vuillot, F., Avalon, G., Plourde, F., Anthoine, J., and Platet, B., “Use of cold flow experiments in the ASSM program - Lessons and results,” *2nd European Symposium on Launcher Technology*, Rome, Italy, 2000.

[9] Anthoine, J., Buchlin, J.-M., and Hirschberg, A., “Effect of nozzle cavity on resonance in large SRM: theoretical modeling,” *Journal of Propulsion and Power*, Vol. 18, No. 2, 2002, pp. 304–311.

[10] Anthoine, J. and Olivari, D., “Cold flow simulation of vortex induced oscillations in a model of solid propellant boosters,” *Proceedings of the 5th AIAA/CEAS Aeroacoustics Conference*, Greater Seattle, Washington, AIAA Paper 99–1826, 1999.

[11] Anthoine, J., Repellin, O., Buchlin, J.-M., and D., O., “The Ariane–5 MPS aeroacoustics research at VKI: an overview,” *Proceedings of the 1st European Symposium on Launcher Technology*, Toulouse, France, 1999, pp. 569–578.

[12] Anthoine, J., Yildiz, D., and Buchlin, J.-M., “Nozzle geometry effect on the instabilities in a radial injected cold flow model of solid propellant boosters,” *Proceedings of the 2nd European Symposium on Launcher Technology, Space Solid Propulsion*, Rome, Italy, 2000.

[13] Yildiz, D., Anthoine, J., and Buchlin, J.-M., “Influence of radial injected flow on the aeroacoustic coupling in solid propellant boosters,” *Proceedings of the 7th AIAA/CEAS Aeroacoustics Conference*, Maastricht, The Netherlands, AIAA Paper 2001-2101, May 2001.

[14] Anthoine, J., Olivari, D., Hulshoff, S., and Van Rooij, M., “Qualitative model of vortex induced oscillations in a model of solid propellant boosters,” *Proceedings of the 4th AIAA/CEAS Aeroacoustics Conference*, Toulouse, France, AIAA Paper 98–2270, 1998.

[15] Anthoine, J., Planquart, P., Olivari, D., Van Rooij, M., and Hulshoff, S., “Génération de bruit dans les moteurs à propergol solide,” *Proceedings of the 3ème Colloque R&T CNES/ONERA “Ecoulements Internes en Propulsion Solide”*, ENSMA, Futuroscope, Poitiers, France, 1998.

[16] Anthoine, J. and Olivari, D., “Cold flow simulation of vortex induced oscillations in a model of solid propellant boosters,” AIAA Paper 99–1826, 1999.

[17] Rossiter, J. E., “Wind tunnel experiments on the flow over rectangular cavities at subsonic and transonic speeds,” Aeronautical Research Council, Ministry of Aviation, Reports and Memoranda 3438, London, 1964.

[18] Hourigan, K., Welsh, M. C., Thompson, M. C., and Stokes, A. N., “Aerodynamic sources of acoustic resonance in a duct with baffles,” *Journal of Fluids and Structures*, Vol. 4, 1990, pp. 345–370.

[19] Hirschberg, A., Hulshoff, S., van Hassel R. R., and Anthoine, J., “Vortex-acoustic interaction in internal flows: the Whistler-nozzle, human whistling and the solid-propellant rocket motor,” *Proceedings of the 3ème Colloque R&T CNES/ONERA “Ecoulements Internes en Propulsion Solide”*, ENSMA, Futuroscope, Poitiers, France, 1998.

[20] Michalke, A., “On the inviscid instability of the hyperbolic-tangent velocity profile,” *Journal of Fluid Mechanics*, Vol. 19, 1964, pp. 543–556.

[21] Crow, S. C. and Champagne, F. H., “Orderly structure in jet turbulence,” *Journal of Fluid Mechanics*, Vol. 48, No. 3, 1971, pp. 547–591.

[22] Tso, J., Kovasznay, L. S. G., and Hussain, A. K. M. F., “Search for large-scale coherent structures in the nearly self-preserving region of a turbulent axisymmetric jet,” *Journal of Fluids Engineering - Transactions of the ASME*, Vol. 103, 1981, pp. 503–508.

[23] Gurevich, M. I., *Theory of jets in ideal fluids*, Academic Press, 1965.

[24] Rockwell, D. and Naudascher, E., “Self-sustained oscillations of flow past cavities,” *Journal of Fluids Engineering*, Vol. 100, 1978, pp. 152–165.

[25] Bruggeman, J. C., Hirschberg, A., van Dongen, M. E. H., and Wijnands, A. P. J., “Self-sustained aero-acoustic pulsations in gas transport systems: experimental study of the influence of closed side branches,” *Journal of Sound and Vibrations*, Vol. 150, No. 3, 1991, pp. 371–393.

[26] Flechter, N. H. and Rossing, T., *The physics of musical instruments*, Springer-Verlag, NY, 2nd ed., 1998.

[27] Verge, M. P., Causé, R., Fabre, B., Hirschberg, A., Wijnands, A. P. J., and Steenbergen, A., “Jet oscillations and jet drive in recorder-like instruments,” *Acta Acustica*, Vol. 2, 1994, pp. 403–419.

[28] Mettenleiter, M., *Contrôle adaptatif des propulseurs segmentés*, Ph.D. thesis, Ecole Centrale Paris, February 2000.

[29] Anthoine, J., Buchlin, J.-M., and Guéry, J.-F., "Experimental and numerical investigations of nozzle geometry effect on the instabilities in solid propellant boosters," AIAA Paper 2000–3560, 2000.

[30] Anthoine, J., Mettenleiter, M., Repellin, O., Buchlin, J.-M., and Candel, S., "Influence of adaptive control on vortex driven instabilities in a scaled model of solid propellant motors," *Journal of Sound and Vibration*, 2001, accepted for publication.

[31] Powell, A., "Theory of vortex sound," *Journal of Acoustical Society of America*, Vol. 36, No. 1, 1964, pp. 177–195.

[32] Howe, M. S., "Contributions to the theory of aerodynamic sound, with application to excess jet noise and the theory of the flute," *Journal of Fluid Mechanics*, Vol. 71, 1975, pp. 625–673.

[33] Vuillot, F., Tissier, P. Y., and De Amicis, R., "Stability prediction for large segmented solid propellant rocket motors," *Proceedings of the AAAF, 5ème Symposium International sur la Propulsion dans les Transports Spatiaux*, Paris, France, 1996.

[34] Avalon, *Private communication*, 2007.

[35] Putman, A. A., *Combustion driven oscillations in industry*, Fuel and Energy Science Series. J.M. Beer Ed. American Elsevier N-Y., 1971.

[36] Sohn, C. H. and Park, I. S., "Acoustic Tuning of Gas-Liquid Scheme Injectors for Acoustic Absorption in a Rocket Combustor," AIAA Paper 2006–4723, 2006.

[37] Lawrence, E. K. and Austin, R. F., *Fundamentals of acoustics*, John Wiley & Sons, 1962.

This page has been purposedly left blank